

Theory of unconventional superconductivity in nickelate-based materials

Ming Zhang(张铭), Yu Zhang(张渝), Huaiming Guo(郭怀明), and Fan Yang(杨帆)

Citation: Chin. Phys. B, 2021, 30 (**10**): 108204. DOI: 10.1088/1674-1056/ac0bb1
Journal homepage: http://cpb.iphy.ac.cn; http://iopscience.iop.org/cpb

What follows is a list of articles you may be interested in

Hard carbons derived from pine nut shells as anode materials for Na-ion batteries

Hao Guo(郭浩), Kai Sun(孙凯), Yaxiang Lu(陆雅翔), Hongliang Wang(王洪亮), Xiaobai Ma(马小柏), Zhengyao Li(李正耀), Yong-Sheng Hu(胡勇胜), Dongfeng Chen(陈东风)

Chin. Phys. B, 2019, 28 (**6**): 068203. DOI: 10.1088/1674-1056/28/6/068203

New layered metal oxides as positive electrode materials for room-temperature sodium-ion batteries

Mu Lin-Qin, Hu Yong-Sheng, Chen Li-Quan

Chin. Phys. B, 2015, 24 (**3**): 038202. DOI: 10.1088/1674-1056/24/3/038202

Novel copper redox-based cathode materials for room-temperature sodium-ion batteries

Xu Shu-Yin, Wu Xiao-Yan, Li Yun-Ming, Hu Yong-Sheng, Chen Li-Quan

Chin. Phys. B, 2014, 23 (**11**): 118202. DOI: 10.1088/1674-1056/23/11/118202

Spinel lithium titanate ($Li_4Ti_5O_{12}$) as novel anode material for room-temperature sodium-ion battery

Zhao Liang,Pan Hui-Lin,Hu Yong-Sheng,Li Hong,Chen Li-Quan

Chin. Phys. B, 2012, 21 (**2**): 028201. DOI: 10.1088/1674-1056/21/2/028201

SPECIAL TOPIC — Unconventional superconductivity

Theory of unconventional superconductivity in nickelate-based materials*

Ming Zhang(张铭)[1], Yu Zhang(张渝)[2], Huaiming Guo(郭怀明)[3,†], and Fan Yang(杨帆)[1,‡]

[1] School of Physics, Beijing Institute of Technology, Beijing 100081, China
[2] Institute for Quantum Science and Engineering and Department of Physics, Southern University of Science and Technology, Shenzhen 518055, China
[3] School of Physics, Beihang University, Beijing 100191, China

(Received 26 February 2021; revised manuscript received 30 May 2021; accepted manuscript online 16 June 2021)

Based on the two-band tight-binding model composed of the 3d orbital of Ni and the 5d orbital of R (= La), we used the random-phase-approximation method to study the pairing symmetry of the nickelate superconductors. It is found that even without considering the coupling between the R and Ni orbitals, neither the antiferromagnetic spin-fluctuation pattern nor the doping-dependent behavior of the robust $d_{x^2-y^2}$-wave pairing state obtained in our calculations will be obviously influenced. Our results suggest the dominating role of the Ni 3d orbital in determining the low lying physics of the system. Furthermore, our results reveal a dome-shaped doping dependence of the superconducting transition temperature T_c, which is consistent with recent experiments.

Keywords: nickelate superconductor, pairing symmetries

PACS: 82.47.Cb, 74.78.−w, 74.25.Dw **DOI:** 10.1088/1674-1056/ac0bb1

1. Introduction

The discovery of superconductivity (SC) with highest T_c up to 15 K in the Sr-doped infinite-layer nickelate $NdNiO_2$[1,2] has attracted great research interests both experimentally[3–7] and theoretically.[4,8–26] This superconductor was thought to be a Ni-based analogy of the hight-temperature cuprates superconductors:[2] the $3d^9$ electronic configuration of the Ni^+ in the $NdNiO_2$ is similar to that of the Cu^{2+} in the cuprates; both compounds have isostructural CuO_2/NiO_2 plane with D_4 symmetry. Density functional theory (DFT) based calculations[12] suggest that the electron–phonon coupling mediated pairing mechanism cannot account for the T_c as high as 15 K, and the SC in this material is more likely driven by electron–electron interactions. More remarkably, recent doping study over the parent compound reveals a dome-shaped dependence of the superconducting T_c over the doping concentration,[5,6] which is similar to that of the cuprates. These similarities between the Sr-doped $NdNiO_2$ and the cuprates superconductors imply that the study on the former is helpful for the clarification of the pairing mechanism of the high-temperature cuprate superconductors.[27]

There are, however, significant differences between the cuprates and the infinite-layer nickelate.[2] One difference lies in the presence of the small Fermi-pockets around the A- and possibly the Γ-points in the Brillouin zone in the parent compound $NdNiO_2$, which are mainly contributed from the 5d electrons of the Nd.[8,11–14,19,22–26] These Nd 5d-state-originated Fermi pockets lead to self doping into the should-be Mott-insulating NiO_2 plane with extra holes. Note that the charge-transfer gap between the Ni 3d states and the O 2p states in the $NdNiO_2$ is much larger than that in the cuprates,[2,7,9,21,24] which indicts that the extra holes in the NiO_2 plane should locate on the Ni 3d orbitals instead of the O 2p ones. Therefore, the Zhang–Rice singlet[28] present in the cuprates is absent here. These conducting Nd 5d electrons and the extra holes in the NiO_2 plane make the $NdNiO_2$ metallic. The other obvious difference lies in that, unlike the cuprates, the parent compound $NdNiO_2$ is not antiferromagnetic (AFM) ordered.[2,29,30] One possible reason lies in that the AFM superexchange interaction in the $NdNiO_2$ is much weaker than that in the cuprates.[2,7] The other reason lies in that the Kondo coupling between the conduction Nd 5d electrons and the localized Ni 3d electrons leads to formation of the Kondo singlet at low temperature,[2,13,14,16,23,24] which suppresses the AFM order. Therefore, the main difference between the cuprates and the infinite-layer nickelate might lies in the presence of the low-lying Nd 5d degree of freedom in the parent compound. Such difference will be largely suppressed with the enhancement of the hole doping,[11,12,15,25] as the participation of the Nd 5d electrons in the low-energy physics simply takes the form of electron pockets, which will vanish or shrink upon hole doping. Therefore, as long as the pairing mechanism and pairing symmetry in the Sr-doped compound are considered, the Ni 3d electrons should take the main role.

*Project supported by the National Natural Science Foundation of China (Grant Nos. 12074031, 11674025, and 11774019).
†Corresponding author. E-mail: hmguo@buaa.edu.cn
‡Corresponding author. E-mail: yangfan_blg@bit.edu.cn
© 2021 Chinese Physical Society and IOP Publishing Ltd

The band structure of the $NdNiO_2$ has been studied previously.[31–33] To make the succeeding calculations considering electron–electron interactions realizable, a tight-binding (TB) model with finite-range hopping integrals is required. In the TB model introduced in Ref. [22], all the orbitals involved on the FS are considered, which leads to a seven- or six-orbital model. Such a model can provide a perfect description of the band structure of $NdNiO_2$. Then a fluctuation-exchange study on this model yields the $d_{x^2-y^2}$ pairing symmetry. Here to make the physics more simple and clear, we start from a two-orbital TB model provided in Ref. [4]. In this model, only the Nd 5d orbital and the Ni $3d_{x^2-y^2}$ orbital are considered. As the hybridization between the two orbitals is weak,[4] we perform two comparison studies on the model: in one study we adopt the realistic band structure with weak coupling between the two orbitals, in the other one we turn off the coupling and study the imaginary comparison model. Our random-phase-approximation (RPA) based calculations yield very similar results for the two studies: both studies yield the $d_{x^2-y^2}$ pairing symmetry consistent with that obtained in other studies,[11,22,24] and the spin correlations obtained in the two studies are very similar: both studies reveal strong in-plane spin fluctuations, consistent with Refs. [17,20]. In both studies, either the Cooper pairing or the spin fluctuations are mainly carried out by the Ni $3d_{x^2-y^2}$ orbital. Our results suggest that the Sr-doped $NdNiO_2$ superconductor is essentially a single Ni-$3d_{x^2-y^2}$-orbital system, and the only role of the Nd 5d orbital is to slightly tune the doping concentration of the charge carrier. More interestingly, our study can well reproduce the dome-shaped dependence of the T_c over the Sr-doping concentration revealed in the recent experiment,[5,6] implying the relevance of our study to the real material.

The rest of this paper is organized as follows. In Section 2, we describe the adopted TB model. In Section 3, we introduce the details of the RPA approach engaged in our calculations. In Section 4, we provide the results of our numerical calculations: we study both cases of realistic $V^{R,\mathrm{Ni}} \neq 0$ and imaginary $V^{R,\mathrm{Ni}} = 0$ for comparison. Here $V^{R,\mathrm{Ni}}$ (R = La,Nd) represents the hybridization between the Ni-$3d_{x^2-y^2}$ orbital and the R-5d orbital. It will be seen that the two cases yield very similar results, and that the Ni-$3d_{x^2-y^2}$ orbital takes the main role in determining the low-energy physics of the system. Finally, in Section 5, conclusions are reached with further discussions.

2. The model

The $RNiO_2$ (R = La, Nd) has a body-centered cubic structure with the lattice constants $a = b \neq c$. In the cubic unit cell, R (Ni) is at the vertex (center) of the cube, and O is in the middle of each face. The band structures of $LaNiO_2$ and $NdNiO_2$ are very similar, in which only the $3d_{x^2-y^2}$ orbital of Ni and the 5d orbitals of La or Nd play the main role near the Fermi energy.[4,11] Here we start from a minimal two-band tight binding model[4] to describe the low-energy physics dominated by the rare-earth R and Ni bands, which writes as

$$H_0 = \sum_{k,\sigma}(\varepsilon_k^R n_{k\sigma}^R + \varepsilon_k^{\mathrm{Ni}} n_{k\sigma}^{\mathrm{Ni}}) + \sum_{k,i,\sigma}(V_{k,k'} c_{k,\sigma}^{+} d_{k',\sigma} + \mathrm{h.c.}), \quad (1)$$

where $c_{k,\sigma}^{\dagger}$ ($c_{k,\sigma}$) and $d_{k,\sigma}^{\dagger}$ ($d_{k,\sigma}$) are the creation (annihilation) operators for an electron with the momentum k and spin $\sigma = \uparrow, \downarrow$ of the R and Ni subsystems, respectively; $V_{kk'}$ represents the coupling strength between the R and Ni bands; $n_{k\sigma}^R = c_{k,\sigma}^{\dagger} c_{k,\sigma}$ and $n_{k\sigma}^{\mathrm{Ni}} = d_{k,\sigma}^{\dagger} d_{k,\sigma}$ are the number operators; ε_k^R and $\varepsilon_k^{\mathrm{Ni}}$ describes the single-particle energy spectra of the R and Ni bands, respectively. Note that in the electron picture adopted here, the positive Sr-doping represents negative doping values in this model.

We take the relevant parameters from Ref. [4], and show the band structure of the Hamiltonian (1) in Fig. 1. Note that although the provided TB parameters are for $LaNiO_2$, the obtained band structure can also well describe the band structure of $NdNiO_2$, as the band structures of the two materials are very similar. Here only the Ni $3d_{x^2-y^2}$ and La $5d_{3z^2-r^2}$ orbitals are considered for simplicity. In this system, although the Ni 3d orbital and the La 5d orbital are coupled through hybridization, such coupling is on the order of $O(10^{-2})$ eV, which is negligibly small compared to the intra-layer hopping amplitudes. Therefore, each of the two resulting bands has a dominating orbital component. The Ni 3d-orbital dominated band is almost dispersionless along Γ–Z (z-axis in the Brillouin zone), and hence it is of two-dimensional (2D) nature. In contrast, the La 5d-orbital dominated band is quite

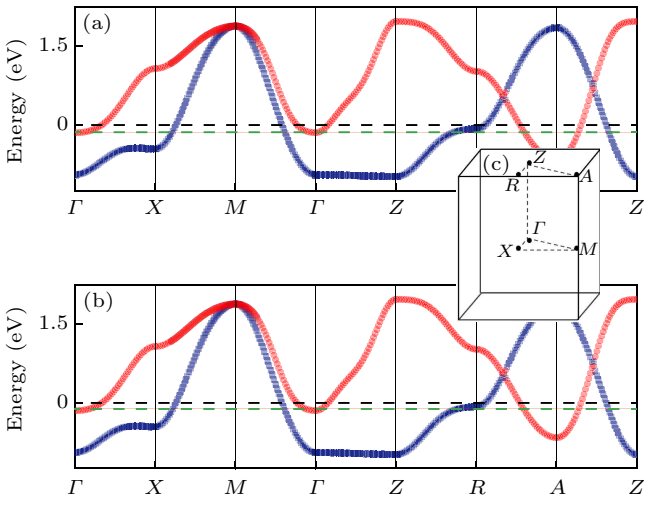


Fig. 1. Band structure of the Hamiltonian in Eq. (1): (a) the realistic case with weak inter-orbital coupling; (b) the comparison case with the inter-orbital coupling turning off. In (a) ((b)), the red one is mainly (completely) composed of R 5d, and the blue one is mainly (completely) composed of Ni $3d_{x^2-y^2}$. (c) The high symmetry points in the tetragonal Brillouin zone. The two dashed lines are the chemical potentials corresponding to doping 0 and doping −0.2, respectively.

extended and three-dimensional (3D). Specially two small Fermi surface pockets are formed at the Γ and the A points, based on this 3D band. For comparison purpose, we also calculate the band structure with the inter-orbital hybridization turning off, i.e., $V_{kk'} = 0$, in which the two bands are completely decoupled. As shown in Fig. 1(b), the resulting band structure is almost identical to that in Fig. 1(a), and all features are remained.

The density of states (DOS) of the system is shown in Fig. 2(a), with the contributions from the two orbital components marked separately. From Fig. 2(a), it is clear that for the undoped parent compound, the most part of the DOS is contributed by the Ni $3d_{x^2-y^2}$ orbital, with the R 5d orbital slightly contributing to the DOS. Further more, when the compound is hole-doped by substituting some R^{3+} ions with Sr^{2+} atoms, the part contributed by the R 5d orbital continues decreasing and vanishes promptly. On the contrary, the part of the DOS contributed by the Ni $3d_{x^2-y^2}$ orbital increases promptly upon the hole-doping, and experiences a 3D VHS (introduced below) at the doping $\delta_c = -0.1$. After that the DOS decreases, leading to a dome-shaped curve for the DOS contributed by the Ni $3d_{x^2-y^2}$ orbital, as shown in Fig. 2(a). When the parent compound is electron-doped, the situation becomes very different: the part of the DOS contributed by the Ni $3d_{x^2-y^2}$ orbital decreases promptly, while that contributed by the R 5d orbital orbital increases. The DOS for the comparison model with the inter-orbital coupling turning off is shown in Fig. 2(b), which can not be obviously distinguished from Fig. 2(a).

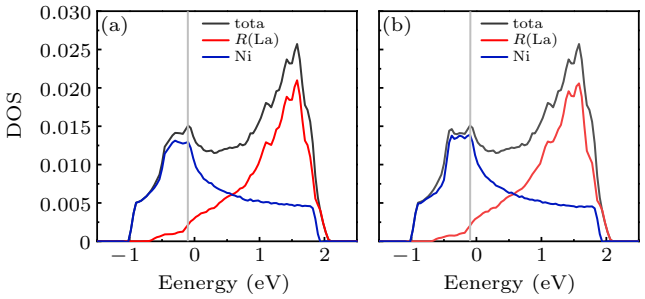


Fig. 2. DOS of the Hamiltonian in Eq. (1): (a) the realistic case; (b) the comparison case. The contribution to the DOS from each orbital component is also marked, with the red one marking the La 5d component and the blue one marking the Ni $3d_{x^2-y^2}$ one. The grey vertical line marks the VH doping level, which is equal to -0.1 for (a) and -0.11 for (b).

The 3D Fermi surface (FS) of the model is shown in Fig. 3(a) for the undoped parent compound and Fig. 3(b) for the hole-doped case with doping level $\delta = -0.2$ where the T_c of the SC is the highest. For the zero doping, the FS includes a 2D columnar sheet centering around the M–A line whose main orbital component is the Ni 3d orbital, and two 3D spherical Fermi pockets centering around the Γ and the A points respectively whose main orbital component is the R 5d orbital. While the Ni-3d-orbital derived 2D FS column is hole pocket, the two R-5d-orbital derived pockets are electron pockets. For $\delta = -0.2$, the two electron pockets contributed mainly from the R-5d-orbital greatly shrink, with the Γ pocket nearly invisible. In the meantime, the columnar "hole pocket" formed mainly by the Ni-3d-orbital expands obviously with hole-doping until its top part near the $k_z = \pi$ plane experiences a Lifshitz transition and changes its topology, as is more clear in the 2D FS shown below.

The 3D FSs for the comparison band structure with the inter-orbital coupling between the Ni 3d and R-5d-orbitals turning off are shown in Fig. 3(c) for the undoped case and Fig. 3(d) for $\delta = -0.2$, which cannot be obviously distinguished from the uncoupled case shown in Figs. 3(a) and 3(b).

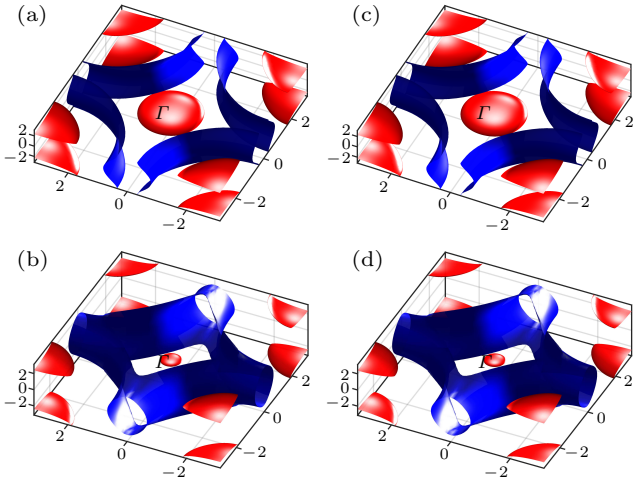


Fig. 3. The 3D FSs for the realistic band structure at the doping levels (a) $\delta = 0$ and (b) $\delta = -0.2$; and those for the comparison band structure at the doping levels (c) $\delta = 0$ and (d) $\delta = -0.2$.

The 2D FS for the zero doping is shown in Fig. 4(a) for $k_z = 0$ and 4(b) for $k_z = \pi$, while that for the doping level $\delta = -0.2$ is shown in Figs. 4(c) and 4(d). Figures 4(a) and 4(b) reveal the two separate R 5d-orbital derived 3D electron pockets centering at the Γ and A points, and the Ni 3d-orbital derived 2D columnar FS surrounding the M–A line which can be regarded as a hole pocket. Clearly, the cut of this Ni 3d pocket on the $k_z = \pi$ plane hosts a larger area than that on the $k_z = 0$ plane. When the doping is shifted to $\delta = -0.2$, the two R 5d-orbital derived 3D electron pockets shrink a lot, with the Γ-pocket almost invisible. In the meantime, the Ni 3d pocket expands a lot, as shown by Figs. 4(c) and 4(d). Such expansion is more clear on the $k_z = \pi$ plane, where the different sheets of the hole pocket which used to surround the A point at $\delta = 0$ now touch with each other and the FS on this plane has now changed to an electron pocket surrounding the Z point. Such a FS-topology change on the $k_z = \pi$ plane suggests that the system has experienced a Lifshitz transition, which takes place at the doping level $\delta_c = -0.1$. Such a Lifshitz transition makes a van Hove singularity (VHS), with the VH momenta locating at the R-points. Such a VHS on the FS has enhanced the DOS, leading to a broad peak in the DOS curve shown in Fig. 2. The 2D FS and its evolution with doping for the comparison band structure with the inter-orbital coupling turning off (un-shown) cannot be obviously distinguished from Fig. 4.

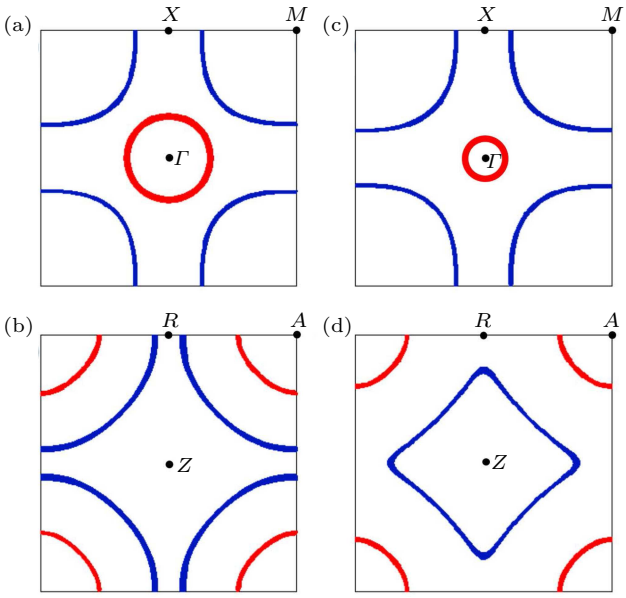


Fig. 4. The 2D FSs for the doping levels $\delta = 0$ on the $k_z = 0$ plane (a) and $k_z = \pi$ plane (b), and those for the doping levels $\delta = -0.2$ on the $k_z = 0$ plane (c) and $k_z = \pi$ plane (d). Only the results for the realistic band structure are shown.

3. The RPA formulation

We then consider the on-site Hubbard interaction on the Ni $d_{x^2-y^2}$ orbital, which writes as

$$H_{\text{int}} = U\sum_i n_{i\uparrow}^{\text{Ni}} n_{i\downarrow}^{\text{Ni}}. \tag{2}$$

Note that we have omitted the interaction term on the R 5d orbital, as the Hubbard interaction for the 5d orbital of R (R = La, Nd) is much weaker than that for the 3d orbital of Ni. The total Hamiltonian $H = H_0 + H_{\text{int}}$ is treated within the weak coupling approach: random-phase approximation (RPA). In the standard RPA approach for a multiband model,[34–43] the bare susceptibility for a particle–hole excitation is defined as

$$\chi_{st}^{(0)pq}(\boldsymbol{q}, \mathrm{i}\omega_n) \equiv \frac{1}{N}\sum_{\boldsymbol{r}\boldsymbol{r}'} \mathrm{e}^{\mathrm{i}\boldsymbol{q}\cdot(\boldsymbol{r}-\boldsymbol{r}')} \int_0^\beta \mathrm{e}^{\mathrm{i}\omega_n\tau}\mathrm{d}\tau \left\langle c_p^\dagger(\boldsymbol{r},\tau) c_q(\boldsymbol{r},\tau) \times c_s^\dagger(\boldsymbol{r}',0) c_t(\boldsymbol{r}',0)\right\rangle_0, \tag{3}$$

where $\langle\cdots\rangle_0$ represents the expectation value in the free-electron state; $\boldsymbol{r}$ and $\boldsymbol{r}'$ are the space positions, and $p,q,s,t = 1,2$ are the orbital indices. Here the orbital indices 1 and 2 denote the R 5d orbital and the Ni $3d_{x^2-y^2}$ orbital, respectively. Transforming the above electron operators to the momentum space, we obtain

$$\chi_{st}^{(0)pq}(\boldsymbol{q}, \mathrm{i}\omega_n) \equiv \frac{1}{N}\sum_{\boldsymbol{k}_1\boldsymbol{k}_2} \int_0^\beta \mathrm{e}^{\mathrm{i}\omega_n\tau}\mathrm{d}\tau \left\langle \mathrm{e}^{\tau H} c_p^\dagger(\boldsymbol{k}_1,0) c_q(\boldsymbol{k}_1+\boldsymbol{q},0) \times \mathrm{e}^{-\tau H} c_s^\dagger(\boldsymbol{k}_2,0) c_t(\boldsymbol{k}_2-\boldsymbol{q},0)\right\rangle_0, \tag{4}$$

with $\boldsymbol{k}_1$ and $\boldsymbol{k}_2$ the wave vectors. We then perform a unitary transformation to the diagonal basis,

$$c_t(\boldsymbol{k}) = \sum_{\tilde{t}} \gamma_{t\tilde{t}}(\boldsymbol{k}) c_{\tilde{t}}(\boldsymbol{k}), \tag{5}$$

where $\tilde{t}$ is a band index. The expression in Eq. (4) becomes

$$\begin{aligned}&\chi_{st}^{(0)pq}(\boldsymbol{q}, \mathrm{i}\omega_n) \\ &\equiv \frac{1}{N}\sum_{\boldsymbol{k}_1\boldsymbol{k}_2} \int_0^\beta \mathrm{e}^{\mathrm{i}\omega_n\tau}\mathrm{d}\tau \\ &\quad\times \sum_{\tilde{p}\tilde{q}\tilde{s}\tilde{t}} \gamma_{\tilde{p}p}^*(\boldsymbol{k}_1)\gamma_{\tilde{q}q}(\boldsymbol{k}_1+\boldsymbol{q})\gamma_{\tilde{s}s}^*(\boldsymbol{k}_2)\gamma_{\tilde{t}t}(\boldsymbol{k}_1-\boldsymbol{q}) \\ &\quad\times \left\langle \mathrm{e}^{\tau H} c_{\tilde{p}}^\dagger(\boldsymbol{k}_1,0) c_{\tilde{q}}(\boldsymbol{k}_1+\boldsymbol{q},0)\, \mathrm{e}^{-\tau H} c_{\tilde{s}}^\dagger(\boldsymbol{k}_2,0) c_{\tilde{t}}(\boldsymbol{k}_2-\boldsymbol{q},0)\right\rangle_0.\end{aligned} \tag{6}$$

Integrating out β and using the Wick's theorem, the bare susceptibility is expressed explicitly as

$$\chi_{st}^{(0)pq}(\boldsymbol{q}, \mathrm{i}\omega_n) = \frac{1}{N}\sum_{\boldsymbol{k}_1\alpha\beta} \gamma_{\alpha p}^*(\boldsymbol{k}_1)\gamma_{\beta q}(\boldsymbol{k}_1+\boldsymbol{q})\gamma_{\beta s}^*(\boldsymbol{k}_1+\boldsymbol{q})\gamma_{\alpha t}(\boldsymbol{k}_1) \times \frac{f(\varepsilon_{\boldsymbol{k}_1+\boldsymbol{q}}^\beta - \mu_{\text{c}}) - f(\varepsilon_{\boldsymbol{k}_1}^\alpha - \mu_{\text{c}})}{\mathrm{i}\omega_n + \varepsilon_{\boldsymbol{k}_1}^\alpha - \varepsilon_{\boldsymbol{k}_1+\boldsymbol{q}}^\beta}, \tag{7}$$

where $\alpha,\beta = 1,2$ represent the band indices; $\varepsilon_{\boldsymbol{k}}^\alpha$ is the α-th eigenvalue of the $H_0(\boldsymbol{k})$ matrix; μ_{c} is the chemical potential, and $f(\varepsilon_{\boldsymbol{k}}) = 1/(1+\mathrm{e}^{\beta\varepsilon_{\boldsymbol{k}}})$ is the Fermi–Dirac distribution function.

When the Hubbard interaction in Eq. (2) is included, we can explicitly calculate the spin and charge susceptibilities. In the RPA level, the renormalized spin and charge susceptibilities of the system read

$$\chi^{(s/c)}(\boldsymbol{k}, \mathrm{i}w_n) = \left[I \mp \chi^{(0)}(\boldsymbol{k}, \mathrm{i}w_n) U^{s/c}\right]^{-1} \chi^{(0)}(\boldsymbol{k}, \mathrm{i}w_n). \tag{8}$$

Here the nonzero elements $U_{\theta\xi}^{(s/c)\mu\nu}$ of U^s are as follows:

$$U_{\theta\xi}^{(s)/(c)\mu\nu} = U\delta_{\mu=\nu=\theta=\xi=2}. \tag{9}$$

Generally, repulsive Hubbard interactions suppress the charge susceptibility, but enhance the spin susceptibility.[34–46] There is a critical interaction strength U_{c}, where the spin susceptibility diverges, indicating that the long-range magnetic order forms, and the RPA treatment is no longer valid.[47–50,52] When the interaction strength is below U_{c}, short-ranged spin and charge fluctuations exist in the system. Electrons may form Cooper pairs by exchanging these fluctuations, resulting in exotic superconducting states in the system.

We consider the scattering of a Cooper pair from the state $(\boldsymbol{k}', -\boldsymbol{k}')$ in the β-th band to the state $(\boldsymbol{k}, -\boldsymbol{k})$ in the α-th band via exchanging spin or charge fluctuations. This second-order perturbation process will contribute an effective interaction vertex $\Gamma_{pq}^{st}(\boldsymbol{k},\boldsymbol{k}')$. Considering only intraband pairings, we project the effective interaction $\Gamma_{pq}^{st}(\boldsymbol{k},\boldsymbol{k}')$ onto the FSs and obtain an effective pairing potential $V^{\alpha\beta}(\boldsymbol{k},\boldsymbol{k}')$. The explicit formulas of $\Gamma_{pq}^{st}(\boldsymbol{k},\boldsymbol{k}')$ and $V^{\alpha\beta}(\boldsymbol{k},\boldsymbol{k}')$ are given in Appendix B. Following such a procedure, we obtain the effective Hamiltonian

$$H_{\text{eff}} = \sum_{\boldsymbol{k},\alpha,\sigma} \varepsilon_{\boldsymbol{k}}^\alpha c_{\alpha\sigma}^\dagger(\boldsymbol{k}) c_{\alpha\sigma}(\boldsymbol{k})$$

$$+\frac{1}{N}\sum_{\boldsymbol{k}\boldsymbol{k}',\alpha\beta}V^{\alpha\beta}\left(\boldsymbol{k},\boldsymbol{k}'\right)c^{\dagger}_{\alpha\uparrow}(\boldsymbol{k})c^{\dagger}_{\alpha\downarrow}(-\boldsymbol{k})c_{\beta\downarrow}\left(-\boldsymbol{k}'\right)c_{\beta\uparrow}\left(\boldsymbol{k}'\right). \tag{10}$$

In the mean-field approximation, the interaction term is decoupled as

$$\begin{aligned}&\frac{1}{N}\sum_{\boldsymbol{k}\boldsymbol{k}',\alpha\beta}V^{\alpha\beta}\left(\boldsymbol{k},\boldsymbol{k}'\right)c^{\dagger}_{\alpha\uparrow}(\boldsymbol{k})c^{\dagger}_{\alpha\downarrow}(-\boldsymbol{k})c_{\beta\downarrow}\left(-\boldsymbol{k}'\right)c_{\beta\uparrow}\left(\boldsymbol{k}'\right)\\&=\sum_{\boldsymbol{k},\alpha}\left(\Delta^{\alpha}_{\boldsymbol{k}}c^{\dagger}_{\alpha\uparrow}(\boldsymbol{k})c^{\dagger}_{\alpha\downarrow}(-\boldsymbol{k})+\text{h.c.}\right),\end{aligned} \tag{11}$$

which causes the energy gap equation

$$\Delta^{\alpha}_{\boldsymbol{k}}=\frac{1}{N}\sum_{\boldsymbol{k}',\beta}V^{\alpha\beta}\left(\boldsymbol{k},\boldsymbol{k}'\right)\left\langle c_{\beta\downarrow}\left(-\boldsymbol{k}'\right)c_{\beta\uparrow}\left(\boldsymbol{k}'\right)\right\rangle. \tag{12}$$

The Hamiltonian in Eq. (10) becomes

$$\begin{aligned}H_{\text{mf}}=&\sum_{\boldsymbol{k},\alpha,\sigma}\varepsilon^{\alpha}_{\boldsymbol{k}}c^{\dagger}_{\alpha\sigma}(\boldsymbol{k})c_{\alpha\sigma}(\boldsymbol{k})\\&+\sum_{\boldsymbol{k},\alpha}\left(\Delta^{\alpha}_{\boldsymbol{k}}c^{\dagger}_{\alpha\uparrow}(\boldsymbol{k})c^{\dagger}_{\alpha\downarrow}(-\boldsymbol{k})+\text{h.c.}\right).\end{aligned} \tag{13}$$

Under the Bogliubov transformation

$$\begin{aligned}c_{\alpha\uparrow}(\boldsymbol{k})=&u_{\alpha}(\boldsymbol{k})\gamma_{\alpha\uparrow}(\boldsymbol{k})+v_{\alpha}(\boldsymbol{k})\gamma^{\dagger}_{\alpha\downarrow}(-\boldsymbol{k}),\\c_{\alpha\downarrow}(-\boldsymbol{k})=&u_{\alpha}(\boldsymbol{k})\gamma_{\alpha\downarrow}(-\boldsymbol{k})-v_{\alpha}(\boldsymbol{k})\gamma^{\dagger}_{\alpha\uparrow}(-\boldsymbol{k}),\\u^2_{\alpha}(\boldsymbol{k})=&\frac{1}{2}\left(1+\frac{\varepsilon^{\alpha}_{\boldsymbol{k}}}{\xi^{\alpha}_{\boldsymbol{k}}}\right),\\v^2_{\alpha}(\boldsymbol{k})=&\frac{1}{2}\left(1-\frac{\varepsilon^{\alpha}_{\boldsymbol{k}}}{\xi^{\alpha}_{\boldsymbol{k}}}\right),\\\xi^{\alpha}_{\boldsymbol{k}}=&\sqrt{(\varepsilon^{\alpha}_{\boldsymbol{k}})^2+\left|\Delta^{\alpha}_{\boldsymbol{k}}\right|^2},\end{aligned} \tag{14}$$

the mean-field Hamiltonian becomes diagonal, and the gap equation becomes

$$\begin{aligned}\Delta^{\alpha}_{\boldsymbol{k}}=&-\frac{1}{N}\sum_{\boldsymbol{k}',\beta}V^{\alpha\beta}\left(\boldsymbol{k},\boldsymbol{k}'\right)\frac{\Delta^{\beta}_{\boldsymbol{k}'}}{2\xi_{\boldsymbol{k}'}}\left[1-2f(\xi_{\boldsymbol{k}'})\right]\\=&-\frac{1}{(2\pi)^2}\sum_{\beta}\int\mathrm{d}k'_{\parallel}\int\mathrm{d}k'_{\perp}V^{\alpha\beta}\left(\boldsymbol{k},\boldsymbol{k}'\right)\frac{\Delta^{\beta}_{\boldsymbol{k}'}}{2\xi^{\beta}_{\boldsymbol{k}'}}\tanh\left(\frac{\xi^{\beta}_{\boldsymbol{k}'}}{2k_{\text{B}}T}\right).\end{aligned} \tag{15}$$

It is noted that the main contribution to the above integration comes from the momenta near the Fermi surface where $\varepsilon^{\alpha}_{\boldsymbol{k}}=v^{\alpha}_{\text{F}}(\boldsymbol{k})k_{\perp}$.

Near the superconducting critical temperature T_{c}, $\Delta^{\alpha}_{\boldsymbol{k}}$ tends to be zero. Up to the first-order term of $\Delta^{\alpha}_{\boldsymbol{k}}$, the $|\Delta^{\alpha}_{\boldsymbol{k}}|^2$ is omitted and the integration over $k_{\perp}$ can be worked out as

$$\begin{aligned}&\int\mathrm{d}k'_{\perp}\frac{1}{2\left|\varepsilon^{\beta}_{\boldsymbol{k}'}\right|}\tanh\left(\frac{\left|\varepsilon^{\beta}_{\boldsymbol{k}'}\right|}{2k_{\text{B}}T_{\text{c}}}\right)\\=&\frac{1}{v^{\beta}_{\text{F}}\left(\boldsymbol{k}'\right)}\int_{-\hbar\omega_{\text{D}}}^{\hbar\omega_{\text{D}}}\mathrm{d}\varepsilon^{\beta}_{\boldsymbol{k}'}\frac{1}{2\left|\varepsilon^{\beta}_{\boldsymbol{k}'}\right|}\tanh\left(\frac{\left|\varepsilon^{\beta}_{\boldsymbol{k}'}\right|}{2k_{\text{B}}T_{\text{c}}}\right)\\=&\frac{1}{v^{\beta}_{\text{F}}\left(\boldsymbol{k}'\right)}\ln\left(1.13\frac{\hbar\omega_{\text{D}}}{k_{\text{B}}T_{\text{c}}}\right).\end{aligned} \tag{16}$$

The Eq. (12) becomes the following linearized one:[38,39]

$$-\frac{1}{(2\pi)^2}\sum_{\beta}\oint_{\text{FS}}\mathrm{d}^2k'_{\parallel}\frac{V^{\alpha\beta}(\boldsymbol{k},\boldsymbol{k}')}{v^{\beta}_{\text{F}}(\boldsymbol{k}')}\Delta_{\beta}(\boldsymbol{k}')=\lambda\Delta_{\alpha}(\boldsymbol{k}), \tag{17}$$

with $\lambda^{-1}=\ln\left(1.13\frac{\hbar\omega_{\text{D}}}{k_{\text{B}}T_{\text{c}}}\right)$ and ω_{D} the Debye frequency. Here the integration is along various FS patches labelled by α or β, $v^{\beta}_{\text{F}}(\boldsymbol{k}')$ is the Fermi velocity, and $\boldsymbol{k}'_{\parallel}$ is the component of $\boldsymbol{k}'$ along the FS. Solving this gap equation as an eigenvalue problem, one obtains each pairing eigenvalue λ and the corresponding normalized eigenvector $\Delta_{\alpha}(\boldsymbol{k})$ as the relative pairing gap function. The leading pairing symmetry is determined by the $\Delta_{\alpha}(\boldsymbol{k})$ corresponding to the largest λ. The critical temperature T_{c} is determined by λ through $T_{\text{c}}=$ cutoff energy $\times\,\text{e}^{-1/\lambda}$, where the cutoff energy scales with the low energy bandwidth.

According to the D_{4h} point group[53] of $LaNiO_2$, the possible superconducting pairing symmetries include $A_{1g}(s)$-, $E_u(p)$-, B_{1g} ($d_{x^2-y^2}$)-, B_{2g} (d_{xy})-, A_{2g} ($d_{x^2-y^2}\times d_{xy}$)-, $A_{2u}(p_z)$-, $E_g(p_x\times p_z/p_y\times p_z)$-, B_{2u} ($d_{x^2-y^2}\times p_z$)-, B_{1u} ($d_{xy}\times p_z$)- and A_{1u} ($d_{x^2-y^2}\times d_{xy}\times p_z$)-wave ones. The eigenvector(s) $\Delta_{\alpha}(\boldsymbol{k})$ for each eigenvalue λ obtained from gap equation (17) as the basis function(s) forms (form) an irreducible representation of the D_{4h} point group. While the $E_u(p)$, E_g ($p_x\times p_z/p_y\times p_z$) symmetries each form a 2D representation with degenerate pairing eigenvalues, other symmetries each forms a 1D representation of the point group with nondegenerate pairing eigenvalues. The character table for each representation of the D_{4h} point group is shown in Table 1.

Table 1. The D_{4h} character table.

	E	σ_{xz}	σ_{yz}	$\sigma_{(x=y),z}$	$\sigma_{(x=-y),z}$	C^1_4	C^2_4	C^3_4	σ_{xy}	$\sigma_{xz}\sigma_{xy}$	$\sigma_{yz}\sigma_{xy}$	$\sigma_{(x=y),z}\sigma_{xy}$	$\sigma_{(x=-y),z}\sigma_{xy}$	$C^1_4\sigma_{xy}$	$C^2_4\sigma_{xy}$	$C^3_4\sigma_{xy}$
s (A_{1g})	1	1	1	1	1	1	1	1	1	1	1	1	1	1	1	1
p_x/p_y (E_u)	2	0	0	0	0	0	−2	0	2	0	0	0	0	0	−2	0
$d_{x^2-y^2}$ (B_{1g})	1	1	1	−1	−1	−1	1	−1	1	1	1	−1	−1	−1	1	−1
d_{xy} (B_{2g})	1	−1	−1	1	1	−1	1	−1	1	−1	−1	1	1	−1	1	−1
$d_{x^2-y^2}\cdot d_{xy}$ (A_{2g})	1	−1	−1	−1	−1	1	1	1	1	−1	−1	−1	−1	1	1	1
p_z (A_{2u})	1	1	1	1	1	1	1	1	−1	−1	−1	−1	−1	−1	−1	−1
$p_x\cdot p_z/p_y\cdot p_z$ (E_g)	2	0	0	0	0	0	−2	0	−2	0	0	0	0	0	2	0
$d_{x^2-y^2}\cdot p_z$ (B_{2u})	1	1	1	−1	−1	−1	1	−1	−1	−1	−1	1	1	1	−1	1
$d_{xy}\cdot p_z$ (B_{1u})	1	−1	−1	1	1	−1	1	−1	−1	1	1	−1	−1	1	−1	1
$d_{x^2-y^2}\cdot d_{xy}\cdot p_z$ (A_{1u})	1	−1	−1	−1	−1	1	1	1	−1	1	1	1	1	−1	−1	−1

4. Numerical result

In this section, we present our numerical results for the spin correlations and pairing symmetries in this system. We compare the results obtained for two cases: one case is for the realistic band structure with weak inter-orbital coupling between the Ni 3d and La 5d orbitals, and the other one is for the imaginary comparison band structure with no coupling between the Ni 3d and La 5d orbitals. Our results suggest that the spin correlations obtained for the two cases are similar, and the pairing symmetries obtained are both $d_{x^2-y^2}$ which is robust against doping. Our results suggest that the pairing mechanism and pairing symmetry of this system are mainly determined by the 3d orbital of Ni, and the main role of La is only to adjust the effective doping concentration. In the following, we provide our results for both cases simultaneously. For the doping levels, we provide two cases for comparison: one is zero doping, and the other is -0.2 which represents a typical doping level with obvious T_c for the SC. The 3D and 2D FSs for the two doping levels are shown in Figs. 3 and 4, respectively.

In Fig. 5, we show the $\boldsymbol{k}$ dependence of the susceptibility $\chi(\boldsymbol{k})$ in the Brillouin zone. Here χ represents the largest eigenvalue of the susceptibility matrix (χ). The element $\chi_{lm}(\boldsymbol{k})$ of this matrix is defined as

$$\chi_{lm}(\boldsymbol{k}) \equiv \chi^{(0)ll}_{mm}(\boldsymbol{k}, \mathrm{i}\omega_n = 0). \tag{18}$$

Here $\chi^{(0)ll}_{mm}(\boldsymbol{k}, \mathrm{i}\omega_n = 0)$ is the element of the susceptibility tensor $\chi^{(0)}(\boldsymbol{k}, \mathrm{i}\omega_n = 0)$ defined in Eq. (3), whose explicit formula is given by Eq. (7) by setting $\mathrm{i}\omega_n = 0$. Note that in the comparison model with the inter-orbital coupling turned off, the matrix $\chi_{lm}(\boldsymbol{k})$ is diagonal: $\chi_{lm}(\boldsymbol{k}) = \delta_{lm}\chi_{ll}(\boldsymbol{k})$ from Eq. (7), because the matrix $\Gamma(\boldsymbol{k})$ appearing in Eq. (7) is diagonal.

The $\chi(\boldsymbol{k})$ for two typical doping levels, i.e., 0 and -0.2, are shown in Fig. 5. For the zero doping, such momentum dependence is shown along the high-symmetry lines in the Brillouin zone in (a), on the $k_z = 0$ plane in (b), and on the $k_z = \pi$ plane in (c). Clearly, there are two peaks for the distribution of $\chi(\boldsymbol{q})$, with one near the $M = (\pi, \pi, 0)$ point, and the other near the $A = (\pi, \pi, \pi)$ point. The in-plane component of both momenta is (π, π), reflecting the strong in-plane antiferromagnetic (AFM) spin correlations. The two peaks are nearly degenerate, reflecting the competition between inter-layer AFM and FM correlations. When the doping concentration is changed to -0.2, such momentum dependence is shown in Figs. 5(d)–5(f). In this doping level, there are still two susceptibility peaks near the M and A points. However, the A-peak is slightly higher than the M-peak, reflecting that while the in-plane spin correlation is still AFM, the inter-layer one is also AFM. Similar $\boldsymbol{k}$ dependence of $\chi(\boldsymbol{k})$ for the comparison band structure with the inter-orbital coupling turning off is shown in Fig. 6. A comparison between Figs. 5 and 6 reveals that the two figures are nearly the same, suggesting that the influence of the inter-orbital coupling between the Ni 3d orbital and the R 5d orbital on the spin correlations in this system can be ignored.

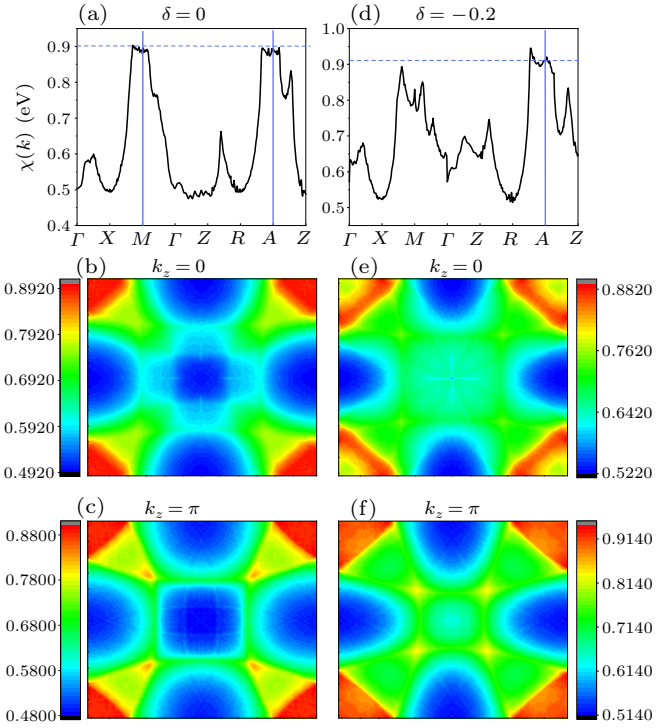


Fig. 5. The $\boldsymbol{k}$-space distribution of the largest eigenvalue $\chi(\boldsymbol{k})$ of the susceptibility matrix for the realistic band structure. Of which, (a), (b), (c) represent the doping 0 and (d), (e), (f) represent the doping -0.2. (a) and (d) are along the high-symmetry lines in the Brillouin zone, (b) and (e) are on the $k_z = 0$ plane, and (c) and (f) are on the $k_z = \pi$ plane.

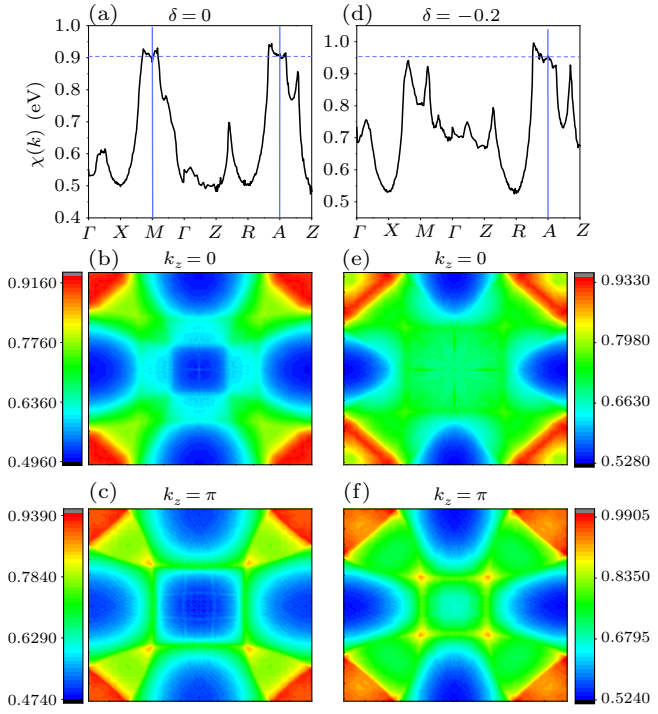


Fig. 6. The $\boldsymbol{k}$-space distribution of the largest eigenvalue $\chi(\boldsymbol{k})$ of the susceptibility matrix for the comparison band structure with the inter-orbital coupling turned off. The meaning of each figure is similar to that in Fig. 5.

From the eigenvector $\xi(\boldsymbol{k}_m)$ corresponding to the largest eigenvalue $\chi(\boldsymbol{k}_m)$ of the susceptibility matrix at $\boldsymbol{k}_m$, the spin fluctuation in the system takes the pattern of $\boldsymbol{s}_{i\mu} = \xi_\mu(\boldsymbol{k}_m)\mathrm{e}^{\mathrm{i}\boldsymbol{k}_m\cdot\boldsymbol{r}_i}$. The spin-fluctuation pattern thus obtained for the doping level $\delta = -0.2$ is shown from top view in Fig. 7(a) and from side view in Fig. 7(b). As the $\boldsymbol{k}_m$ for this doping level is at A, the obtained spin-fluctuation pattern is the Neel-ordered AFM pattern both intra-layer and inter-layer. What's more, the distribution of $\boldsymbol{s}_{i\mu}$ between the two orbitals $\mu = 1$ and $\mu = 2$ is determined by $\xi_\mu(\boldsymbol{k}_m)$. From our calculation, it is obtained as $\xi_1(\boldsymbol{k}_m)/\xi_2(\boldsymbol{k}_m) = 10^{-4}$, which is very small. As a result, the spin fluctuation is mainly carried by the Ni 3d orbital, as shown in Figs. 7(a) and 7(b). Similar spin-fluctuation patterns thus obtained for the comparison case with the coupling between the Ni 3d and the R 5d orbitals turning off are shown in Figs. 7(c) and 7(d) for the top and side views, respectively. In Figs. 7(c) and 7(d), the spin pattern is completely distributed on the Ni 3d orbital as $\xi_1(\boldsymbol{k}_m) = 0, \xi_2(\boldsymbol{k}_m) = 1$, suggesting that if we omitted the inter-orbital coupling the spin fluctuation should be completely carried by the Ni 3d orbital. Comparing the case with realistic weak inter-orbital coupling between the Ni 3d and R 5d orbitals and the one without such inter-orbital coupling, it is known that the spin fluctuation in this system is mainly carried by the Ni 3d orbital and the R 5d orbital only participates into the spin fluctuation through the tiny hybridization with Ni 3d orbital.

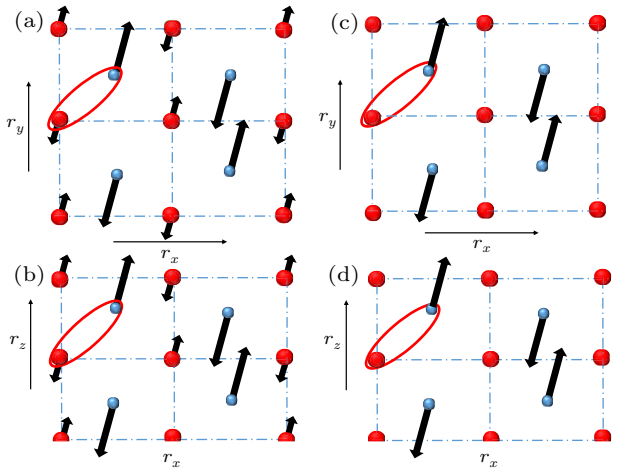


Fig. 7. The spin-fluctuation pattern, in which blue color represents Ni and the red one represents La. (a), (b) are top view and side view for the realistic band structure with weak inter-orbital coupling and (c), (d) are top view and side view for the comparison band structure with the inter-orbital coupling turned off. The doping for both cases is -0.2. The relative ratio between the lengths of the arrows representing the spins of the two orbitals has been exaggerated.

When the interaction strength is below the critical one, the above illustrated spin fluctuation is short-ranged. Through exchanging these short-ranged spin fluctuations, a pair of electrons with opposite momenta can acquire effective attraction and pair, which leads to the SC. In our calculations, we take $U = 0.9$ eV, under which the renormalized spin and charge susceptibilities do not diverge, which suggest that this interaction strength is below the critical one. The pairing phase diagram thus obtained is shown in Fig. 8. Figure 8 suggests that the phase diagram (a) for the realistic band structure with weak inter-orbital coupling between Ni 3d and R 5d and that (b) for the comparison band structure with the inter-orbital coupling turning off are very similar. Figure 8 reveals three experimentally relevant characters in the doping dependence of the pairing phase diagram.

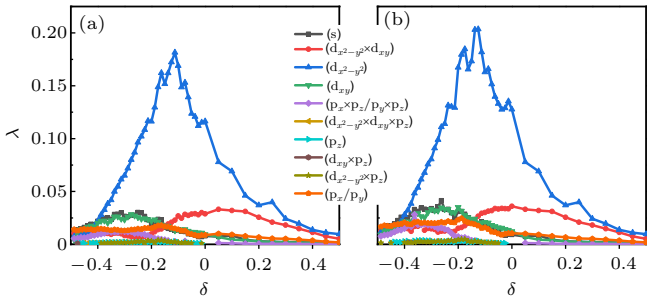


Fig. 8. Doping δ dependence of the largest pairing eigenvalue λ for each pairing symmetry for the realistic band structure (a) and the comparison band structure (b).

Firstly, the pairing T_c for the hole-doped case is much larger than that for the electron-doped case. Particularly, the T_c for the electron-doped case decreases promptly with doping, which might possibly be invisible in experiment. This character is different from that of the cuprates superconductors which host high-temperature SC for both hole-doped and electron-doped cases and is consistent with the experiment of the Sr-doped $NdNiO_2$ superconductors wherein the Sr doping introduced holes into the material. The physical reason in our study for this character lies in that, on the one hand the Ni 3d orbital-component contributes less and less to the DOS of the electron-doped case, and on the other hand it is the Ni 3d orbital-component which contributes to the SC of the material, as more clearly illustrated below. Our study thus predicts that no obvious SC would be detected for the electron-doped case of the $NdNiO_2$.

Secondly, the pairing T_c for the hole-doped case exhibits a dome shape, which peaks in between the doping levels -0.1 and -0.2. Such a dome-shaped curve of the doping-dependent T_c is qualitatively consistent with recent experiments[5,6] wherein the peak of the T_c is near the doping -0.2. The physical reason of this character lies in that, the Ni 3d-orbital component of the DOS, which contributes mainly to the SC of the system, peaks near this doping range, as shown in the DOS curve in Fig. 2. This DOS peak originates from the VHS caused by the Lifshitz transition of the FS, as shown in Fig. 9. Figures 9(a) and 9(b) show the 2D FS on the $k_z = 0$ and $k_z = \pi$ planes for the VH doping $\delta_c = -0.1$ for the realistic band structure. This 2D FS can be compared with those for $\delta = 0$ and $\delta = -0.2$ shown in Fig. 4. Clearly, while the 2D FSs for the three cases on the $k_z = 0$ plane have the same topology, those on the $k_z = \pi$ plane illustrate a FS-topology change. While the FS on the $k_z = \pi$ plane

for $\delta = 0$ shown in Fig. 4(b) comprises a R 5d-orbital derived electron pocket and a Ni 3d-orbital derived hole pocket centering around the A point, that for $\delta = -0.2$ shown in Fig. 4(d) comprises two electron pockets, with the Ni 3d-orbital derived FS sheet now changing topology to an electron pocket centering around the Z point. Clearly, the Ni 3d-orbital derived FS sheet has experienced a Lifshitz transition from $\delta = 0$ to $\delta = -0.2$. Figure 9(b) just illustrates the Lifshitz transition point at $\delta_c = -0.1$, on which the separate FS sheets appearing in Fig. 4(b) now touch with each other at the R-points, making these points as the VH momenta. This 3D VHS will not lead to a divergence of the DOS, but it causes a broad peak in the DOS in Fig. 2(a), which just leads to the broad T_c-peak in Fig. 8(a). The situation for the comparison band structure ($\delta_c = -0.11$) shown in Figs. 9(c) and 9(d) is similar, which is related to the broad T_c-peak in Fig. 8(b).

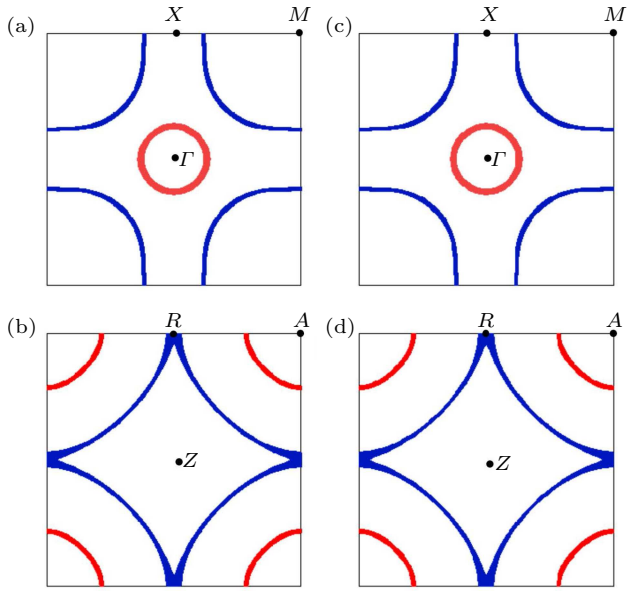


Fig. 9. The 2D FS of the VH doping ($\delta_c = -0.1$) for the realistic band structure on the $k_z = 0$ plane (a) and $k_z = \pi$ plane (b), and that ($\delta_c = -0.11$) for the comparison band structure on the $k_z = 0$ plane (c) and $k_z = \pi$ plane (d).

Thirdly, while all the ten possible pairing symmetries listed in Table 1 are possible, the $d_{x^2-y^2}$-wave pairing dominates over other pairing symmetries in the whole doping range where obvious SC can be detected. This robust $d_{x^2-y^2}$-wave pairing obtained for our simple model is consistent with those obtained for more complicated models.[11,22] The distribution of the gap function for the obtained $d_{x^2-y^2}$-wave pairing on the FS is shown in Fig. 10(a) on the $k_z = 0$ plane and Fig. 10(b) on the $k_z = \pi$ plane for the doping level $\delta = -0.2$. Obviously, this gap function is symmetric about the x and y axes and is antisymmetric about the $x = \pm y$ axes. Four symmetry-protected line nodes are presented in the 3D Brillouin zone whose projections on the xy plane locate on the $x = \pm y$ axes. It is also obvious that the pairing gap is mainly distributed on the Ni 3d-orbital derived FS sheets, with the component on the R 5d-orbital derived FS sheets almost vanished, suggesting the dominating role of the Ni 3d orbital in determining the SC in this system. The situation for the comparison band structure is similar, as shown in Figs. 10(c) and 10(d).

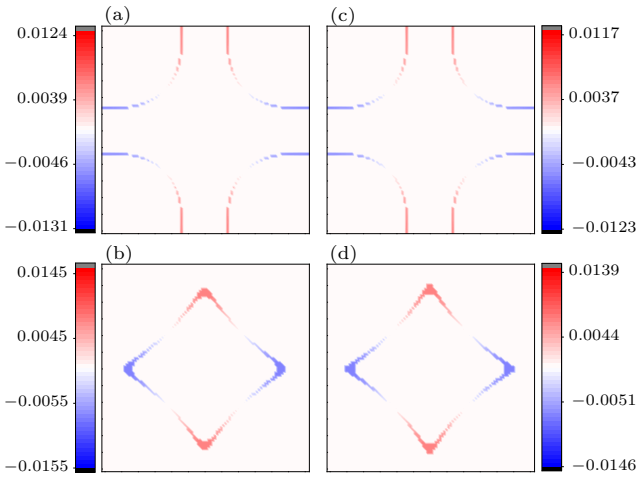


Fig. 10. Distributions of the gap functions on the FS for the doping level −0.2 for the realistic band structure (a), (b) and the comparison band structure with the inter-orbital coupling turned off (c), (d). While (a) and (c) are the distribution on the $k_z = 0$ plane, (b) and (d) represent that on the $k_z = \pi$ plane.

5. Discussion and conclusion

Due to the strong on-site Coulomb interaction between the Ni 3d electrons, the nickelate superconductors might belong to strongly-correlated system, or at least intermediately-correlated one. Here, to avoid the difficulty in the systematic treatment of strongly- or intermediately-correlated electronic systems, we start from the weak-coupling RPA approach, with the adopted Hubbard-U (0.9 eV) several times weaker than the realistic value. Two reasons lie behind this choice of U:[34–43] on the one hand, the RPA as a perturbational approach does not apply to the case with strong U; on the other hand, the condition $U < U_c$ should be satisfied in the RPA approach to avoid divergence of the renormalized susceptibility. Although such choice of the interaction strength will not bring about the accurate value of T_c for a fixed doping level, it is possible to use it to compare the relative values of T_c among different doping levels. Furthermore, the pairing symmetry thus obtained is usually not wrong.

Note that the weak-coupling RPA approach adopted here might have missed the Kondo physics at the small doping levels, where the Kondo coupling between the Ni-3d and the R-5d orbitals might lead to the d + is-wave pairing.[13] However, when the hole-doping levels are large, due to the electron-pocket character of the R-5d dominant FSs, the DOS contributed by the R-5d orbital component is largely reduced, and correspondingly the Kondo physics should be suppressed. Therefore, the conclusion arrived at in our study should only be tenable for large hole-doping concentrations.

In conclusion, we have performed a RPA based calculation for the Sr-doped $RNiO_2$ superconductor, adopting a real-

istic two-band band structure. Through comparison between the results obtained for the realistic band structure and those obtained for the imaginary band structure with the inter-orbital coupling between the Ni 3d and *R* 5d orbitals turned off, it is revealed that the Ni 3d orbital dominates over the *R* 5d orbital in carrying out the AFM spin fluctuation and the superconducting pairing. Our results suggest that this system is essentially a one-orbital (i.e., Ni 3d) system, with the only role of the *R* 5d orbital to slightly tuning the doping concentration in the hole-doped superconducting regime relevant to experiments. Therefore, this material can be well captured by a single-band Hubbard model on the square lattice.

Further more, our results reveal three experimentally relevant doping-dependent behaviors of the pairing state. Firstly, the superconducting pairing is strongly particle–hole asymmetric, with obvious T_c only detectable on the hole-doped side. Secondly, a dome-shaped doping dependence of the SC T_c is obtained, which peaks within the regime of $(-0.2,-0.1)$, qualitatively consistent with recent experiments. These two characters are determined by the doping dependence of the DOS contributed by the Ni 3d orbital, which is particle–hole asymmetric and peaks near the doping regime of $(-0.2,-0.1)$, caused by the 3D VHS. Thirdly, the robust $d_{x^2-y^2}$-wave pairing symmetry dominates over other pairing symmetries in the large doping regime, consistent with the results obtained from other more complicated models.

Acknowledgement

We are grateful to the stimulating discussions with Congjun Wu, Chen Lu, Lun-Hui Hu and Zhan Wang.

Appendix A: Tight-binding forms of $\varepsilon_k^{\mathrm{La}}$ and $\varepsilon_k^{\mathrm{Ni}}$

$$\begin{aligned}
\varepsilon_k^{\mathrm{La}} = {} & \varepsilon_0^{\mathrm{La}} + 2t_{[0,0,1]}^{\mathrm{La}}\cos(k_z) + 2t_{[0,0,2]}^{\mathrm{La}}\cos(2k_z) + 2t_{[0,0,3]}^{\mathrm{La}}\cos(3k_z) \\
& + 2t_{[1,0,0]}^{\mathrm{La}}[\cos(k_x)+\cos(k_y)] \\
& + 4t_{[1,0,1]}^{\mathrm{La}}[\cos(k_x)+\cos(k_y)]\cos(k_z) \\
& + 4t_{[1,0,2]}^{\mathrm{La}}[\cos(k_x)+\cos(k_y)]\cos(2k_z) \\
& + 4t_{[1,1,0]}^{\mathrm{La}}\cos(k_x)\cos(k_y) \\
& + 8t_{[1,1,1]}^{\mathrm{La}}\cos(k_x)\cos(k_y)\cos(k_z) \\
& + 8t_{[1,1,2]}^{\mathrm{La}}\cos(k_x)\cos(k_y)\cos(2k_z) \\
& + 8t_{[1,1,3]}^{\mathrm{La}}\cos(k_x)\cos(k_y)\cos(3k_z) \\
& + 4t_{[2,0,1]}^{\mathrm{La}}[\cos(2k_x)+\cos(2k_y)]\cos(k_z) \\
& + 8t_{[2,1,1]}^{\mathrm{La}}[\cos(2k_x)+\cos(k_y)\cos(k_x)\cos(2k_y)]\cos(k_z), \\
\varepsilon_k^{\mathrm{Ni}} = {} & \varepsilon_0^{\mathrm{Ni}} + 2t_{[1,0,0]}^{\mathrm{Ni}}[\cos(k_x)+\cos(k_y)] + 4t_{[1,1,0]}^{\mathrm{Ni}}\cos(k_x)\cos(k_y) \\
& + 2t_{[2,0,0]}^{\mathrm{Ni}}[\cos(2k_x)+\cos(2k_y)] + 2t_{[0,0,1]}^{\mathrm{Ni}}\cos(k_z) \\
& + 8t_{[1,1,1]}^{\mathrm{Ni}}\cos(k_x)\cos(k_y)\cos(k_z). \qquad \text{(A1)}
\end{aligned}$$

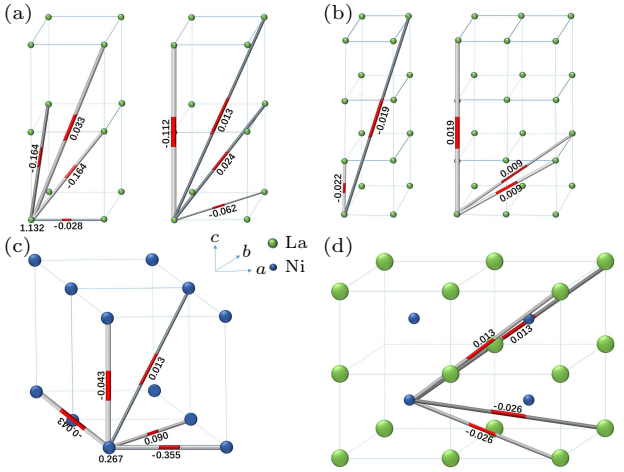


Fig. A1. The hoping between particles in real space, and the unit of related parameters is eV.

Appendix B: The effective interaction

The Feynman's diagram of RPA is shown in Fig. B1. Note that when the interaction strength U is higher than U_c, the denominator matrix $I-\chi^{(0)}(\boldsymbol{k},\mathrm{i}w_n)U^s$ in Eq. (8) will have zero eigenvalues for some $\boldsymbol{q}$ and the renormalized spin susceptibility diverges there, which invalidates the RPA treatment. When $U<U_c$, the short-ranged spin or charge fluctutions would mediate Cooper pairing in the system. Considering a Cooper pair with momentum/orbital $(\boldsymbol{k}'t,-\boldsymbol{k}'s)$, it could be scattered to $(\boldsymbol{k}p,-\boldsymbol{k}q)$ by exchanging charge or spin fluctuations. In the RPA level, the effective interaction induced by this process is as follows:

$$V_{\mathrm{eff}}^{\mathrm{RPA}} = \frac{1}{N}\sum_{pqst,\boldsymbol{k}\boldsymbol{k}'}\Gamma_{pq}^{st}(\boldsymbol{k},\boldsymbol{k}')c_p^+(\boldsymbol{k})c_q^+(-\boldsymbol{k})c_s(-\boldsymbol{k}')c_t(\boldsymbol{k}'). \qquad \text{(B1)}$$

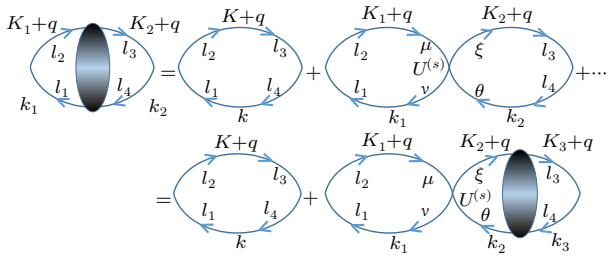


Fig. B1. Feynman's diagram for the renormalized susceptibilities in the RPA level.

We consider the three processes in Fig. B2 which contribute to the effective vertex $\Gamma_{st}^{pq}(\boldsymbol{k},\boldsymbol{k}')$, where (a) represents the bare interaction vertex and (b), (c) represent the two second order perturbation processes during which spin or charge fluctuations are exchanged between a Cooper pair. In the singlet channel, the effective vertex $\Gamma_{st}^{pq}(\boldsymbol{k},\boldsymbol{k}')$ is given as follows:

$$\begin{aligned}
\Gamma_{st}^{pq(s)}(\boldsymbol{k},\boldsymbol{k}') = {} & \left(\frac{U^{(c)}+3U^{(s)}}{4}\right)_{qs}^{pt} \\
& + \frac{1}{4}\left[3U^{(s)}\chi^{(s)}(\boldsymbol{k}-\boldsymbol{k}')U^{(s)} - U^{(c)}\chi^{(c)}(\boldsymbol{k}-\boldsymbol{k}')U^{(c)}\right]_{qs}^{pt}
\end{aligned}$$

$$+\frac{1}{4}\left[3U^{(s)}\chi^{(s)}(\boldsymbol{k}+\boldsymbol{k}')U^{(s)}-U^{(c)}\chi^{(c)}(\boldsymbol{k}+\boldsymbol{k}')U^{(c)}\right]^{ps}_{qt}, \tag{B2}$$

while in the triplet channel, it is

$$\Gamma^{pq(t)}_{st}(\boldsymbol{k},\boldsymbol{k}')=\left(\frac{U^{(c)}-U^{(s)}}{4}\right)^{pt}_{qs}$$
$$-\frac{1}{4}\left[U^{(s)}\chi^{(s)}(\boldsymbol{k}-\boldsymbol{k}')U^{(s)}+U^{(c)}\chi^{(c)}(\boldsymbol{k}-\boldsymbol{k}')U^{(c)}\right]^{pt}_{qs}$$
$$+\frac{1}{4}\left[U^{(s)}\chi^{(s)}(\boldsymbol{k}+\boldsymbol{k}')U^{(s)}U^{(c)}\chi^{(c)}(\boldsymbol{k}+\boldsymbol{k}')U^{(c)}\right]^{ps}_{qt}. \tag{B3}$$

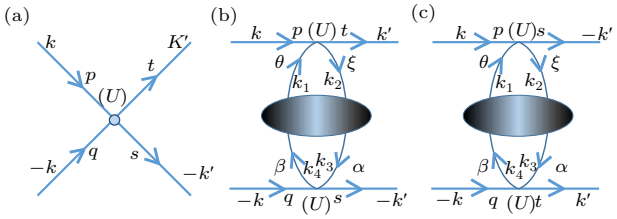


Fig. B2. Three processes which contribute the renormalized effective vertex considered in the RPA, with (a) the bare interaction vertex and (b), (c) the two second order perturbation processes during which spin or charge fluctuations are exchanged between a Cooper pair.

Notice that the vertex $\Gamma^{pq}_{st}(\boldsymbol{k},\boldsymbol{k}')$ has been symmetrized for the singlet case and antisymmetrized for the triplet case. Generally we neglect the frequency dependence of Γ and replace it by $\Gamma^{pq}_{st}(\boldsymbol{k},\boldsymbol{k}')\approx\Gamma^{pq}_{st}(\boldsymbol{k},\boldsymbol{k}',0)$. Usually, only the real part of Γ isadopted.[38,39,52]

Considering only intraband pairings, we obtain the following effective pairing interaction on the FSs:

$$V_{\rm eff}=\frac{1}{N}\sum_{\alpha\beta,kk'}V^{\alpha\beta}(k,k')c^{\dagger}_{\alpha}(k)c^{\dagger}_{\alpha}(-k)c_{\beta}(-k')c_{\beta}(k'), \tag{B4}$$

where $\alpha/\beta=1,2$ are the band indices and $V^{\alpha\beta}(k,k')$ is

$$V^{\alpha\beta}(k,k')=\sum_{pqst,k,k'}\Gamma^{pq}_{st}(k,k',0)\xi^{\alpha,*}_{p}(k)$$
$$\times\xi^{\alpha,*}_{q}(-k)\xi^{\beta}_{s}(-k')\xi^{\beta}_{t}(k'). \tag{B5}$$

From the effective pairing interaction (B4), one can obtain the following linearized gap equation[38,39,51,52] to determine the $T_{\rm c}$ and the leading pairing symmetry of the system:

$$-\frac{1}{(2\pi)^2}\sum_{\beta}\oint_{\rm FS}{\rm d}^2\boldsymbol{k}'_{\parallel}\frac{V^{\alpha\beta}(\boldsymbol{k},\boldsymbol{k}')}{v^{\beta}_{\rm F}(\boldsymbol{k}')}\Delta_{\beta}(\boldsymbol{k}')=\lambda\Delta_{\alpha}(\boldsymbol{k}). \tag{B6}$$

This equation can be looked upon as an eigenvalue problem, where the normalized eigenvector $\delta_{\alpha}(k)$ represents the relative gap function on the α-th FS patches near $T_{\rm c}$, and the eigenvalue λ determines $T_{\rm c}$ via $T_{\rm c}=$ cutoff energy $\times{\rm e}^{-1/\lambda}$, where the cutoff energy is of order bandwidth. The leading pairing symmetry is determined by the largest eigenvalue λ of Eq. (B6).

References

[1] Li D, Lee K, Wang B Y, Osada M, Crossley S, Lee H R, Cui Y, Hikita Y and Hwang H Y 2019 *Nature* **572** 624
[2] Sawasky G A 2019 *Nature* **572** 592
[3] Li K, Goodge B H, Li D, *et al.*, 2020 *APL Material* **8** 041107
[4] Hepting M, Li D, Jia C J, Lu H, Paris E, Tseng Y, Feng X, Osada M, Been E, Hikita Y, Chuang Y D, Hussain Z, Zhou K J, Nag A, Garcia-Fernandez M, Rossi M, Huang H Y, Huang D J, Shen Z X, Schmitt T, Hwang H Y, Moritz B, Zaanen J, Devereaux T P and Lee W S 2020 *Nature Mater.* **19** 381
[5] Li D, Wang B Y, Lee K, *et al.*, 2020 *Phys. Rev. Lett.* **125** 027001
[6] Zeng S, Tang C S, Yin X, *et al.*, 2020 *Phys. Rev. Lett.* **125** 147003
[7] Fu Y, Wang L, Cheng H, *et al.*, 2019 arXiv:1911.03177
[8] Gao J, Peng S, Wang Z, *et al.*, 2019 *Nat. Sci. Rev.* **10** 1093
[9] Hu, L H and Wu C J 2019 *Phys. Rev. Res.* **1** 032046
[10] Jiang P, Si L, Liao Z and Zhong Z 2019 *Phys. Rev. B* **100** 201106(R)
[11] Wu X X, Sante D Di, Schwemmer T, Hanke W, Hanke H Y, Raghu S and Thomale R 2020 *Phys. Rev. B* **101** 060504
[12] Nomura Y, Hirayama M, Tadano T, Yoshimoto Y, Nakamura K and Arita R 2019 *Phys. Rev. B* **100** 205138
[13] Wang Z, Zhang G M, Yang Y F and Zhang F C 2020 *Phys. Rev. B* **102** 220501
[14] Zhang G M, Yang Y F and Zhang F C 2020 *Phys. Rev. B* **101** 020501
[15] Krishna J, LaBollita H, Fumega A O, Pardo V and Botana A S 2020 *Phys. Rev. B* **102** 224506
[16] Choi M Y, Lee K W and Pickett W E 2020 *Phys. Rev. B* **101** 020503(R)
[17] Ryee S, Yoon H, Kim T J, Jeong M Y and Han M J 2020 *Phys. Rev. B* **101** 064513
[18] Lechermann F 2020 *Phys. Rev. X* **10** 041002
[19] Lechermann F 2020 *Phys. Rev. B* **101** 081110(R)
[20] Leonov I, Skornyakov S L and Savrasov S Y 2020 *Phys. Rev. B* **101** 241108(R)
[21] Jiang M, Berciu M and Sawatzky G A 2020 *Phys. Rev. Lett.* **124** 207004
[22] Sakakibara H, Usui H, Suzuki K, *et al.* 2020 *Phys. Rev. Lett.* **125** 077003
[23] Zhang H, Jin L and Wang S 2020 *Phys. Rev. Res.* **2** 013214
[24] Zhang Y H and Vishwanath A 2020 *Phys. Rev. Res.* **2** 023112
[25] Botana A S and Norman M R 2020 *Phys. Rev. X* **10** 011024
[26] Karp J, Botana A S and Norman M R 2020 *Phys. Rev. X* **10** 021061
[27] Lee P A, Nagaosa N and Wen X G 2006 *Rev. Mod. Phys.* **78** 17 (see for example possible mechanism of the hight-temperature cuprates SC)
[28] Zhang F C and Rice T M 1988 *Phys. Rev. B* **37** 3759
[29] Hayward M, Green M, Rosseinsky M and Sloan J 1999 *J. Am. Chem. Soc.* **121** 8843
[30] Hayward M and Rosseinsky M 2003 *Solid State Sci.* **5** 839
[31] Anisimov V I, Bukhvalov D and Rice T M 1999 *Phys. Rev. B* **59** 7901
[32] Lee K W and Pickett W E 2004 *Phys. Rev. B* **70** 165109
[33] Hansmann P, Yang X, Toschi A, Khaliullin G, Andersen O K and Held K 2009 *Phys. Rev. Lett.* **103** 016401
[34] Takimoto T, Hotta T and Ueda K 2004 *Phys. Rev. B* **69** 104504
[35] Yada K and Kontani H 2005 *J. Phys. Soc. Jpn.* **74** 2161
[36] Kubo K 2007 *Phys. Rev. B* **75** 224509
[37] Kuroki K, Onari S, Arita R, Usui H, Tanaka Y, Kontani H and Aoki H 2008 *Phys. Rev. Lett.* **101** 087004
[38] Graser S, Maie T Ar, Hirschfeld P J and Scalapino D J 2009 *New Journal of Physics* **11** 025016
[39] Maier T A, Graser S, Hirschfeld P J and Scalapino D J 2011 *Phys. Rev. B* **83** 100515(R)
[40] Liu F, Liu C C, Wu K, Yang F and Yao Y 2013 *Phys. Rev. Lett.* **111** 066804
[41] Ma T, Yang F, Yao H and Lin H 2014 *Phys. Rev. B* **90** 245114
[42] Zhang L D, Yang F and Yao Y 2015 *Sci. Rep.* **5** 8203
[43] Liu C C, Zhang L D, Chen W Q and Yang F 2018 *Phys. Rev. Lett.* **121** 217001
[44] Kohn W and Luttinger J 1965 *Phys. Rev. Lett.* **15** 524
[45] Raghu S, Kivelson S A and Scalapino D J 2010 *Phys. Rev. B* **81** 224505
[46] Cho W, Thomale R, Raghu S and Kivelson S A 2013 *Phys. Rev. B* **88** 064505
[47] Scalapino D J 2012 *Rev. Mod. Phys.* **84** 1383
[48] Scalapino D J, Loh E and Hirsch J E 1986 *Phys. Rev. B* **34** 8190
[49] Miyake K, Schmitt-Rink S and Varma C M 1986 *Phys. Rev. B* **34** 6554
[50] Lu C, Zhang L D, Wu X, Yang F and Hu J 2018 *Phys. Rev. B* **97** 165110
[51] Zhang L D, Zhang X, Hao J J, Huang W and Yang F 2019 *Phys. Rev. B* **99** 094511
[52] Wu X, Yang F, Le C, Fan H and Hu J 2015 *Phys. Rev. B* **92** 104511
[53] Zingoni A 2019 *International Journal of Solids and Structures* **176** 68